micromachines

MDPI

Article

Uniform Electrodeposition of Ni-Based Diamond Composite Coatings on Inclined Surfaces Using a Conformal Anode and Stepwise-Increasing Current

Haina Liu [1,2], Pingmei Ming [1,*], Wei Yu [1], Chao Wu [1] and Zheng Yang [1]

[1] School of Mechanical and Power Engineering, Henan Polytechnic University, Jiaozuo 454003, China
[2] School of Intelligent Manufacturing and Electrical Engineering, Huanghe Jiaotong University, Jiaozuo 454950, China
* Correspondence: mingpingmei@163.com

Abstract

Electrodeposition of coarse-grit diamond tools with complex profiles is affected by nonuniform current distribution and coating-thickness variations. This study investigated a conformal anode combined with stepwise-increasing current for a 20° inclined working surface. COMSOL Multiphysics 6.4 simulations were performed to evaluate current-density distributions, while grit-free electrodeposition experiments were conducted to assess coating-thickness dispersion. Three current-loading schedules were compared using independently prepared specimens (n = 3 per schedule) under approximately matched nom-inal charge input. In the simulations, the conformal anode reduced the current-density mirror-asymmetry coefficient (AJ) from 11.51% to 1.87%, while the experiments showed a reduction in the coating-thickness coefficient of variation (CVT) from 4.54% to 2.74% within the measured inner region. Among the three schedules, stepwise-increasing cur-rent yielded the lowest mean coefficient of variation in grit number (CVN, 2.04 ± 0.21%) and regional grit-height range (ΔHR, 95.64 ± 1.00 μm). Compared with the constant-cur-rent schedule, the stepwise-increasing-current schedule reduced the grit-fixation duration from 120 to 80.4 min, corresponding to a reduction of approximately 33%. A double-work-ing-surface diamond dressing roller fabricated using the combined process exhibited CVN values of 1.40% and 1.15% on its two working surfaces and a representative ΔHR of 95.45 μm. These results support the feasibility of the proposed approach for the investi-gated geometry, while further evaluation is needed to establish its effects on dressing per-formance.

Keywords: diamond dressing roller; composite electrodeposition; conformal anode; stepwise-increasing current; grit-distribution uniformity

Academic Editor: Youqiang Xing

Received: 28 October 2026
Revised: 27 November 2026
Accepted: 27 November 2026
Published: 29 November 2026

Copyright: © 2026 by the authors. Licensee MDPI, Basel, Switzerland. This article is an open access article distributed under the terms and conditions of the Creative Commons Attribution (CC BY) license.

1. Introduction

Diamond tools are widely used to machine hard and brittle materials such as silicon, silicon carbide, sapphire, and engineering ceramics because of their high hardness, wear resistance, and shape retention [1–3]. Diamond dressing rollers are used for precision profiling of grinding wheels; the quality and profile accuracy of their working layers directly affect the consistency of complex-profile machining. Electrodeposition has been widely

used to fabricate nickel-bonded diamond tools [4]. Nevertheless, variations in the spatial distribution and protruding heights of grits on electroplated diamond tools can affect working-layer topography and machining performance [5,6]. Khosravi et al. [7] investigated a manufacturing approach for diamond profile rollers and related processing conditions to profile accuracy and surface morphology. More recently, Aleksandrova and Mitev [8] investigated the wear resistance of electroplated diamond dressing rollers with mixed grit sizes, highlighting the importance of abrasive-layer characteristics to tool performance. Li et al. [9] used three-dimensional topographic characterization and modeling of electroplated diamond wheels to elucidate the importance of grit size, spatial position, and height distribution. Fang et al. [10] further developed a full-field characterization method for abrasive protrusion heights on electroplated diamond grinding wheels, emphasizing the importance of quantitative surface-topography measurements. For complex working surfaces with inclination or curvature changes, reducing geometry-induced fluctuations in metallic bond-layer thickness and improving the final distribution and height consistency of pre-positioned coarse diamond grits remain important challenges.

Variations in coating thickness on complex surfaces are closely associated with local electrode spacing and current paths determined by working-surface geometry. Existing strategies to regulate cathodic current distribution include conformal anodes, auxiliary cathodes, and insulating shields. Yang and co-workers [11,12] improved the conformity of anode and cathode profiles to reduce variations in coating thickness and alloy composition during the electroforming of complex rotational components. Yang et al. [13] further combined conformal-anode profile optimization, cathodic shielding, and high-frequency pulsed current for alloy electroforming of rotational parts. Zhu et al. [14] optimized anode geometry and associated processing conditions to improve thickness uniformity in rotational nickel components by approximately 60%. More recently, Wang et al. [15] investigated profile-matching anode vibration-assisted electroforming of complex thin-walled components, demonstrating the combined influence of anode geometry and electrolyte flow on coating quality. Mehdizadeh et al. [16] established a theoretical basis for optimizing current distribution using auxiliary electrodes. Park and Park [17], Zhao et al. [18], and Wang et al. [19] employed auxiliary cathodes to alleviate edge-current concentration. Lee et al. [20] reduced the deviation between center and mean current densities on a substrate from approximately 35% to less than 10% using insulating shields. Ahmadkhaniha et al. [21] used simulation and coating measurements on a complex T-shaped structure to examine the relationship between local current density and deposited thickness. Noack et al. [22] combined finite-element electrochemical simulations with experimental measurements to investigate nickel coating-thickness distributions in complex lattice structures. These studies establish useful approaches for regulating current distribution through electrode geometry and boundary conditions, but most focus on continuous metallic layers or microelectroformed structures. Specific evidence for simultaneously regulating metallic coating thickness and coarse-grit fixation on complex surfaces remains limited.

In addition to spatial electric-current distribution, the temporal current-loading schedule influences electrodeposition. Cao et al. [23] compared direct current, pulse, and pulse-reverse electroforming and reported a coating-thickness coefficient of variation of 1.54% under optimized pulse-reverse conditions. More recently, Chen et al. [24] investigated double-pulse nickel electroforming and combined COMSOL simulations with data-driven optimization to improve coating-thickness uniformity. For nickel–diamond systems, Lee et al. [25] showed that current density and pulse frequency affected composite deposition. Yang and Cheng [26] demonstrated that duty cycle and pulse frequency influenced deposit morphology and particle codeposition in Ni–Co–SiC coatings. Zhang et al. [27] examined pulse-electrodeposition parameters for Ni–W–diamond composites. Srimaneerat et al. [28] compared intermittent and continuous pulse-brush plating to assess

particle incorporation in Ni–W/diamond coatings. Sajjadnejad et al. [29] reported the evolution of pulse-electrodeposited Ni/diamond nanocomposite coatings with diamond volume fractions of 0.81–2.24%. Lajevardi et al. [30] adjusted the duty cycle in stages to control the through-thickness particle-content distribution of functionally graded Ni–Al_2O_3 coatings. These studies demonstrate the influence of time-dependent deposition conditions, but predominantly concern suspended micro- or nanoscale particles rather than electrodeposited fixation of pre-positioned coarse diamond grits.

Stage-dependent current loading has also been explored for different stages of metallic deposition. Yang et al. [31] used periodically decreasing current in the overgrowth electroforming of ultra-narrow slit structures. Kim and co-workers [32,33] investigated step-current copper electrodeposition. In an electrolyte containing leveling agents, accelerators, and suppressors, Kim et al. [33] used a low-to-high step-current sequence to fill through-silicon-via-scale trenches without voids, reducing the filling time by approximately 47% relative to the relevant constant-current condition. Shen et al. [34] changed the temporal sequence of stepwise currents at matched nominal charge input and obtained different copper deposit microstructures. These findings support the general concept of adjusting current in stages, but do not establish the influence of an increasing-current schedule on the retention and final height distribution of pre-positioned coarse diamond grits.

Taken together, existing work has shown that electrode geometry and current-loading schedules can each regulate deposition quality. However, systematic comparisons of anode configurations and temporal current paths for inclined working surfaces bearing pre-positioned coarse diamond grits remain limited, especially when metallic coating-thickness dispersion, grit-number distribution, and regional height characteristics are considered together.

This study therefore examines a combined conformal-anode and stepwise-increasing-current approach for uniform electrodeposition of Ni-based diamond composite working layers on inclined surfaces. First, numerical simulations and grit-free deposition controls are used to assess the effects of anode configuration on current distribution and metallic coating-thickness dispersion. Next, under consistent grit-placement and electrolyte-circulation conditions, different current-loading schedules are compared in terms of the final grit-number distribution and regional grit-height range. Finally, the approach is applied to fabricate a double-working-surface diamond dressing roller to assess its applicability to an engineering-scale complex-profile component.

2. Materials and Methods

2.1. Materials and Simplified Experimental Model

A double-working-surface diamond dressing roller with a 40Cr steel substrate was selected as the engineering component. The roller has two symmetric inclined working surfaces, each inclined at 20°, with an included angle of 40° (Figure 1a). The inclination angle was determined by the actual geometry of the selected dressing roller rather than independently optimized in this study. To examine the influence of inclination-induced variations in electrode spacing on current distribution, one working surface was represented by a 40 mm × 20 mm × 2 mm 40Cr steel plate inclined at 20° (Figure 1c). The simplified model isolates the influence of inclined geometry but does not reproduce the curvature, interaction between the two working surfaces, or circumferential effects of the actual roller. Therefore, the results obtained at this inclination may not be directly generalizable to other geometries.

A soluble nickel plate of 99.99% purity, 80 mm × 60 mm in size, served as the anode; insulating tape was used to adjust the effective exposed area. Synthetic diamond grits of

45/50 mesh (300–355 μm) were pre-positioned and subsequently fixed by electrodeposition. The Ni–Co electroplating bath was based on a conventional Watts-type nickel plating solution, with the concentrations of nickel sulfate, nickel chloride, and boric acid selected within the typical ranges reported in GB/T 12332-2008 (ISO 4526:2004) [35]. Cobalt sulfate was introduced for Ni–Co alloy electrodeposition, while sodium dodecyl sulfate and sodium saccharin were added as a wetting agent and an organic additive, respectively. The bath composition and concentrations are listed in Table 1. The bath temperature was maintained at 50 ± 1 °C, and the pH was monitored using a portable pH meter (LC-PHB-1A, Shanghai Lichen-BX Instrument Technology Co., Ltd., Shanghai, China) and maintained at 4.0 ± 0.1.

Before electrodeposition, the 40Cr steel substrate was mechanically polished, electrolytically degreased, acid-pickled, and activated. The surface was sequentially ground using 400-, 800-, and 1000-grit abrasive papers to remove scratches, oxide, and corrosion products. Reverse-polarity electrolytic degreasing was then conducted at 70 ± 2 °C, comprising 5 min of cathodic degreasing at 5 A/dm^2 followed by 1 min of anodic degreasing at 2 A/dm^2. The degreasing bath contained 20 g/L NaOH, 30 g/L Na_2CO_3, 30 g/L Na_3PO_4, and 5 g/L Na_2SiO_3. Subsequently, the sample was immersed in 20% sulfuric acid for 1 min and activated in 5% hydrochloric acid for 1 min before being transferred promptly to the plating bath to limit reoxidation. The substrate pretreatment sequence followed conventional steel surface preparation practices and the pre-coating quality-control requirements of GB/T 12611-2008 [36]. The specific electrolyte concentrations, current densities, treatment durations, and acid-treatment conditions reported above were adopted from an established experimental procedure rather than prescribed individually by the cited standard.

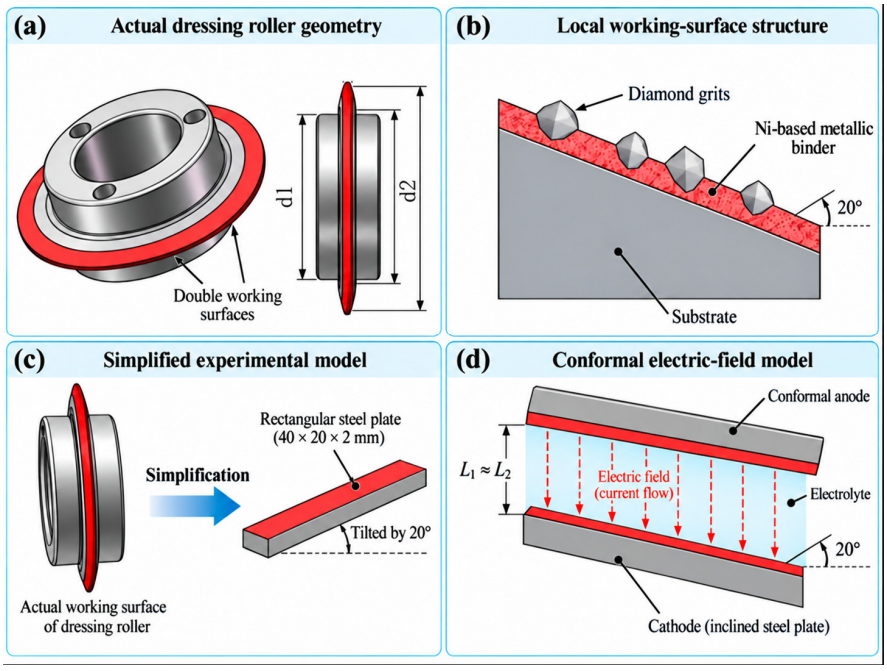


Figure 1. Actual double-working-surface diamond dressing roller and simplified electrodeposition model: (**a**) geometry of the roller; (**b**) structure of the local working layer; (**c**) equivalent 20° inclined steel-plate model; and (**d**) conformal-anode/inclined-cathode configuration. The components and arrows are schematic and not drawn to scale; arrows indicate the nominal current-transfer direction and are not simulated electric-field lines.

Table 1. Composition and concentrations of the electroplating bath.

Component	Chemical Formula	Concentration (g/L)
Nickel sulfate	$NiSO_4 \cdot 6H_2O$	280
Cobalt sulfate	$CoSO_4 \cdot 7H_2O$	20
Nickel chloride	$NiCl_2 \cdot 6H_2O$	35
Boric acid	H_3BO_3	30
Sodium dodecyl sulfate	$CH_3(CH_2)_{11}OSO_3Na$	0.1
Sodium saccharin	$C_7H_4NNaO_3S$	0.5

2.2. Anode Configurations and Numerical Evaluation of Current Distribution

Two electrode configurations were established using the 20° inclined-plate model described in Section 2.1. The conventional configuration comprised a planar anode facing an inclined cathode, producing unequal local electrode gaps along the working surface ($L_1 \neq L_2$). In the conformal configuration, the anode was oriented approximately parallel to the cathodic working surface so that the local gaps approached equality ($L_1 \approx L_2$; Figure 1d). Both configurations used a nominal interelectrode distance of 60 mm. A position coordinate, s, was defined along the 40 mm cathodic working surface.

Numerical simulations were performed using the Electric Currents (ec) interface in COMSOL Multiphysics 6.4 (COMSOL AB, Stockholm, Sweden) under two-dimensional, steady-state Ohmic-conduction conditions. The models were initially established in version 6.3, and the subsequent mesh-sensitivity calculations and data exports were performed using version 6.4. The electrolyte was modeled as a homogeneous and isotropic conductor with an assumed electrical conductivity of 1 S/m. The out-of-plane thickness was set to 1 m in the two-dimensional models. The cathode was grounded, a total current of 1 A was applied at the anode terminal, and the remaining boundaries were electrically insulated. These numerical settings were used to compare the relative current distributions of the two electrode configurations rather than to reproduce the actual electroplating current or predict the absolute deposition rate. The model neglected electrode polarization, concentration variations, Ni/Co codeposition, shielding effects of diamond grits, and interfacial growth.

Physics-controlled triangular meshes were employed at three levels, denoted as M1 (fine), M2 (extra fine), and M3 (extremely fine). The conventional-anode model contained 2045, 6062, and 23,588 triangular elements, respectively, whereas the conformal-anode model contained 2025, 6018, and 23,582 elements. The fine mesh (M1) was used to obtain the current-density profiles, calculate the reported current-density asymmetry coefficients (AJ), and extract the simulated current-density values for comparison with experimental measurements. The M2 and M3 meshes were used to evaluate mesh sensitivity. To facilitate comparison of the relative current-density distributions between different anode configurations, the normalized current density, $\tilde{J}(s)$, was defined as

$$\tilde{J}(s) = \frac{J(s)}{\bar{J}} \tag{1}$$

where the mean current density over the entire working surface was calculated as:

$$\bar{J} = \frac{1}{L}\int_0^L J(s)ds \tag{2}$$

Here, $J(s)$ represents the current density at position s along the cathode working surface, $\bar{J}$ denotes the mean current density over the entire working surface, and L = 40 mm

is the length of the cathode working surface. The normalized current density, $J(s)$, is dimensionless and characterizes the relative spatial current-density distribution for each anode configuration.

To quantitatively evaluate the asymmetry of the current-density distribution along the inclined working surface, a current-density asymmetry coefficient, A_J, was introduced:

$$A_J = \frac{\int_5^{20} |J(s) - J(40-s)| d_s}{\int_5^{20} \frac{J(s)+J(40-s)}{2} d_s} \times 100\% \quad (3)$$

where $J(s)$ and $J(L\text{-}s)$ denote the current densities at two positions symmetrically located about the midpoint of the working surface, $s = L/2$. The current densities at corresponding mirror-symmetric positions were compared over the interval s = 5–20 mm to evaluate the asymmetry associated with the inclined geometry. A smaller A_J indicates a more symmetric current-density distribution within the selected paired regions. It should be noted that this coefficient characterizes only the degree of mirror asymmetry and does not represent the overall uniformity of the current-density distribution across the entire working surface. Therefore, the complete current-density profiles were also examined to assess current crowding near the two electrode edges.

2.3. Current-Loading Profiles and Comparison Under Approximately Equal Nominal Charge

To compare the final spatial distributions of preplaced coarse diamond grits under different current-loading profiles, all experimental groups were prepared under consistent baseline electrodeposition conditions. A conformal-anode configuration was employed, with the effective cathode-to-anode area ratio maintained at 1:2. For each inclined plate, 5 g of diamond grits was uniformly distributed over the 40 mm × 20 mm working surface, corresponding to a nominal grit loading of 62.5 g/dm^2. The electrolyte was circulated using a magnetic-drive pump (MP-15R, Shanghai Xinxishan Industrial Co., Ltd., Shanghai, China), and the flow velocity at the pump outlet was defined as the nominal circulation velocity.

This parameter was used to characterize the intensity of electrolyte circulation and did not represent the instantaneous local flow velocity near the working surface. Preliminary process screening compared horizontal and inclined grit-placement methods, as well as three nominal circulation velocities of 0.5, 1.5, and 2.5 m/s. For the subsequent comparison of current-loading profiles, inclined grit placement matching the 20° working surface and a nominal circulation velocity of 1.5 m/s were consistently employed.

Before grit placement, all specimens were subjected to preliminary electrodeposition at a constant current density of 1.0 A/dm^2 for 37.5 min, followed by grit placement and electrodeposition-assisted grit fixation. To minimize differences in the nominal electrical charge supplied during the fixation stage, three current-loading profiles—constant current, stepwise-increasing current, and step-change current—were designed according to the principle of approximately equal nominal charge per unit area. The corresponding current-density–time profiles are illustrated in Figure 2. The electrodeposition current was supplied using a DC regulated power supply (TRK-325D, Shenzhen Zhaoxin Electronic Instruments and Equipment Co., Ltd., Shenzhen, China).

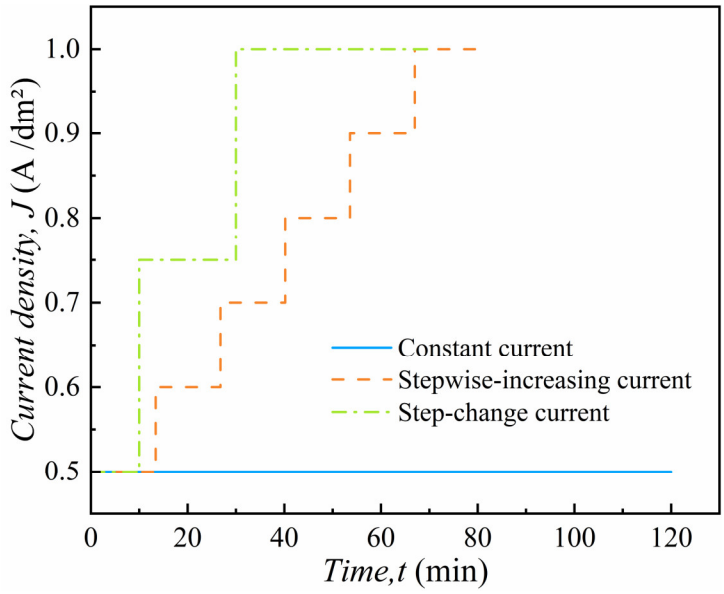


Figure 2. Current-density–time profiles for the three current-loading profiles.

For the constant-current profile, the current density was maintained at 0.5 A/dm² throughout the fixation stage for 120 min. The stepwise-increasing-current profile consisted of six successive current-density levels of 0.5, 0.6, 0.7, 0.8, 0.9, and 1.0 A/dm², each applied for 13.4 min, resulting in a total loading time of 80.4 min. The step-change-current profile involved two abrupt current transitions, with current densities of 0.5, 0.75, and 1.0 A/dm² applied for 10, 20, and 40 min, respectively, giving a total loading time of 70 min. The current density was calculated based on the effective exposed cathode area as follows:

$$J(\mathrm{t}) = \frac{I(t)}{A_{eff}} \tag{4}$$

where $J(t)$ is the time-dependent cathodic current density, $I(t)$ is the applied current, and A_{eff} is the nominal exposed cathode working-surface area used to determine the applied current, without subtracting the projected area occupied by diamond grits.

To quantitatively compare the nominal charge supplied under the three current-loading profiles, the charge passed per unit area was calculated as:

$$q = \frac{1}{60}\int_0^{t_f} J(t)dt = \frac{1}{60}\sum_{k=1}^{n} J_k \Delta t_k \tag{5}$$

where q is the charge passed per unit area, in A·h/dm², t_f is the total loading time (min), J_k and Δt_k are the current density and duration of the k-th loading stage, respectively, and n is the total number of loading stages. The factor of 1/60 converts the time unit from minutes to hours.

Based on the prescribed loading parameters, the nominal charge passed per unit area was 1.000, 1.005, and 1.000 A·h/dm² for the constant-current, stepwise-increasing-current, and step-change-current profiles, respectively. The individual stages contributed 0.112, 0.134, 0.156, 0.179, 0.201, and 0.223 A·h/dm² for stepwise-increasing-current loading, and 0.083, 0.250, and 0.667 A·h/dm² for step-change-current loading, respectively. The maximum relative difference was approximately 0.5%, satisfying the approximately equal nominal-charge criterion adopted in this study. It should be emphasized that the total loading time and average current density differed among the three profiles. Moreover, approximately equal nominal charge does not necessarily imply identical current efficiency, deposited metal mass, or deposit composition. Therefore, this study focused on

comparing the final regional grit distributions and height characteristics obtained under the different current-loading conditions, without attributing the observed differences exclusively to the temporal variation in current density.

After the grit-fixation stage, excess diamond grits were removed from the flat-plate specimens while they remained immersed in the electrolyte. All specimens were subsequently thickened at a constant current density of 1.0 A/dm² for 8 h. This duration followed the flat-plate processing procedure used in the preliminary experiments and was selected to further embed the retained diamond grits before final characterization. Identical thickening conditions were applied to all three current-loading groups to ensure consistent post-fixation processing. Three independently prepared specimens were evaluated for each current-loading schedule (n = 3), giving a total of nine specimens under consistent grit-placement and nominal circulation conditions.

2.4. Fabrication of the Double-Sided Diamond Dressing Roller

An unplated double-working-surface diamond dressing roller substrate supplied by Henan Ruifeng Diamond Products Co., Ltd., Luohe, China, was used to assess the practical applicability of the combined approach. The working surface had an outer diameter of 135 mm, an inner diameter of 115 mm, and a single-surface inclination of 20°. A conformal anode was adapted to the two inclined surfaces, and the stepwise-increasing-current schedule from Section 2.3 was applied during grit placement and initial fixation.

Because the roller had two symmetric working surfaces, the two sides were processed sequentially using alternating grit-placement positions. During fixation on one side, the other working surface and nonworking regions were insulated. The roller was repositioned and the same fixation procedure repeated for the second side. After both sides had been treated, overall thickening was performed at constant current. The current-density calculation used the nominal projected annular working-surface area determined by the inner and outer diameters, without subtracting the area occupied by diamond grits. The area was 39.27 cm² per side and 78.54 cm² in total. Thickening was carried out for 20.5 h at a nominal current density of 1.0 A/dm², corresponding to an applied current of approximately 0.785 A based on the total projected working-surface area. An embedment ratio of approximately 70% of the mean diamond grit size (327.5 μm) was adopted as the process-design target, corresponding to a nominal embedment depth of 229.25 μm. For reference, a simplified Faraday-law estimate based on the nominal current density and a preliminary cathodic current efficiency of approximately 91% gives an equivalent deposition rate of approximately 11.2 μm/h over the nominal projected cathode area. Accordingly, 20.5 h corresponds to an equivalent deposition thickness of approximately 230 μm. This estimate was used as a preliminary reference for selecting the thickening duration. The actual grit embedment also depends on metal deposited during the preceding stages and the local current distribution around the diamond grits. During thickening, the roller was rotated by 90° about its axis every 30 min and reversed axially every 120 min to mitigate position-dependent deposition effects.

After electroplating, the roller was heat-treated at 200 °C for 2 h in a furnace (SA2-6-12TP, Zhuode Instrument Equipment (Shanghai) Co., Ltd., Shanghai, China), without evacuation or protective-gas supply, followed by furnace cooling. The treatment was intended to promote hydrogen relief and reduce residual stresses associated with electrodeposition. However, its independent effects on coating properties and grit-retention strength were not evaluated in this study. The experimental configurations and deposition conditions are summarized in Table 2.

Table 2. Summary of experimental configurations and deposition conditions.

Experimental Condition	Anode Configuration	Grit Placement	Flow Velocity (m/s)	Current-Loading Conditions
Grit-free control 1	Conventional	-	-	0.5 A/dm², 120 min
Grit-free control 2	Conformal	-	-	0.5 A/dm², 120 min
Placement screening 1	Conformal	Horizontal	0.5	Constant: 0.5 A/dm², 120 min
Placement screening 2	Conformal	Inclined	0.5	Constant: 0.5 A/dm², 120 min
Circulation screening 1/constant-current baseline	Conformal	Inclined	1.5	Constant: 0.5 A/dm², 120 min
Circulation screening 2	Conformal	Inclined	2.5	Constant: 0.5 A/dm², 120 min
Current-schedule test 1	Conformal	Inclined	1.5	Stepwise increasing: 0.5–1.0 A/dm², 80.4 min
Current-schedule test 2	Conformal	Inclined	1.5	Step change: 0.5–1.0 A/dm², 70 min
Roller fabrication	Conformal	Sequential, two surfaces	-	Stepwise increasing: 80.4 min; thickening: 1.0 A/dm², 20.5 h

Note: The common experimental parameters and deposition stages are described in Sections 2.1–2.4. The grit-free controls and preliminary screening conditions used one specimen per condition (n = 1). The constant-current screening specimen at 1.5 m/s (C3) was included among the three constant-current specimens (C1–C3) and counted only once. The inclined-placement data at 0.5 m/s were also reused for the circulation comparison.

2.5. Spatial Variability Metrics and Surface Topography Characterization

The coefficient of variation of coating thickness (CV_T), coefficient of variation of grit number (CV_N), and regional grit-height range (ΔH_R) were used to characterize metallic coating-thickness dispersion, spatial grit-number dispersion, and local surface-height variation, respectively. These indicators describe differences among positions or measurement regions within individual specimens; they do not quantify reproducibility across independently manufactured specimens.

To evaluate the influence of anode configuration on the spatial distribution of deposited metal thickness, grit-free Ni-based coating experiments were conducted using conventional and conformal anodes. Electrodeposition was performed at a constant current density of 0.5 A/dm² for 120 min. These experiments did not include the preliminary electrodeposition or subsequent thickening stages; therefore, the measured thickness corresponded exclusively to the metallic layer deposited during this stage. A laser scanning confocal microscope (LEXT OLS5100, Olympus Corporation, Tokyo, Japan) was used to characterize the coating surface profile. The coating thickness was determined from the step height between the coated surface and the adjacent uncoated substrate surface, with the latter serving as the height reference. Local coating thicknesses were measured at seven positions along the inclined working surface, corresponding to s = 5, 10, 15, 20, 25, 30, and 35 mm. The spatial variability in coating thickness was evaluated using the coefficient of variation of coating thickness, CV_T, defined as

$$CV_T = \frac{\sigma_T}{\overline{T}} \times 100\% \quad (6)$$

where $\overline{T}$ is the mean thickness and σ_T is the population standard deviation across the seven positions. Because localized current crowding was expected near the sharp cathode edges, the original thickness-measurement scheme focused on the inner region of the working surface. The two 5 mm end regions (s = 0–5 mm and s = 35–40 mm) were not included.

Therefore, CV_T characterizes only the measured inner region rather than the entire 40 mm working surface.

The final distribution of identifiable diamond grits on the composite working layers of the inclined flat-plate specimens was characterized using an automatic vision measuring instrument (AM600CNC, Dongguan Taibike Precision Instruments Co., Ltd., Dongguan, China). Five nonoverlapping measurement regions, each measuring 3 mm × 3 mm, were selected at distances of at least 3 mm from the specimen edges. The number of identifiable diamond grits in each region was determined using consistent counting criteria. The spatial variability in grit count was evaluated using the coefficient of variation of diamond grit count, CV_N, calculated as

$$CV_N = \frac{\sigma_N}{\bar{N}} \times 100\% \tag{7}$$

where $\bar{N}$ and σ_N are the mean and population standard deviation of grit counts across the five regions. A low CV_N indicates similar counts between selected regions but does not rule out clustering within an individual region.

The same population-standard-deviation convention was used for both spatial metrics:

$$\sigma = \sqrt{\frac{1}{n}\sum_{i=1}^{n}(x_i - \bar{x})^2} \tag{8}$$

where x_i is the measured value at the i-th position or region, $\bar{x}$ is the arithmetic mean of the n measurements, and n = 7 and n = 5 for coating-thickness and grit-count measurements, respectively.

To further characterize the local height distribution of the diamond composite working layer, three-dimensional surface topographies of representative regions were acquired using the OLS5100 microscope(Olympus Corporation, Tokyo, Japan). Within each measurement region, the regional grit-height range, ΔH_R, was defined as the difference between the maximum and minimum valid surface heights of the diamond grits:

$$\Delta H_R = H_{max,R} - H_{min,R} \tag{9}$$

where $H_{max,R}$ and $H_{min,R}$ denote the maximum and minimum valid surface heights on diamond grits in the same measurement region. This is a within-region height range, not the true protrusion of an individual grit above the adjacent metallic bond layer; it must not be interpreted as a measure of height uniformity over the entire working surface.

For the current-loading comparison, five nonoverlapping regions were selected on each specimen for grit counting, and CV_N was calculated using the population standard deviation of the regional grit counts. The regional grit-height range (ΔH_R) was determined from one selected interior measurement region on each specimen. For each current-loading schedule, three independently prepared specimens were evaluated (n = 3). The mean and sample standard deviation of CV_N and ΔH_R were calculated from the three corresponding specimen-level values.

The representative height maps in Figure 5a–c were selected from the predefined interior measurement regions to illustrate local grit topography. Consistent measurement-area dimensions, height references, and visualization scales were applied across the three current-loading schedules. The quantitative comparison was based on specimen-level CV_N and ΔH_R values rather than the displayed representative maps.

Scanning electron microscopy (SEM; GeminiSEM 560, Carl Zeiss Microscopy GmbH, Oberkochen, Germany) was additionally employed to characterize the side-view morphologies of the diamond composite working layers. The images were acquired using a

secondary electron detector (SE2) at an accelerating voltage of 10 kV and magnifications ranging from 70× to 300× to examine the overall grit arrangement and local morphology around the grit bases.

3. Results and Discussion

3.1. Influence of the Conformal Anode on Current Distribution

Figure 3 compares the two anode configurations and their simulated current distributions. In the conventional configuration, the local gap between the planar anode and inclined cathode varies along the working surface. With a conformal anode, the two working surfaces are approximately parallel and the variation in interelectrode spacing decreases (Figure 3a,b). The normalized current-density profiles in Figure 3c and the simulated current-density magnitude maps in Figure 3e,f were used to compare the two electrode configurations. The maps were plotted using the same color scale (0–110 A/m^2).

As shown in Figure 3c, both configurations exhibit edge-current concentration at the two ends of the cathodic working surface. However, the conventional configuration displays substantially greater left–right asymmetry. The conformal anode reduces the difference between mirror-paired current densities, decreasing A_J from 11.51% to 1.87%. This improvement can be explained by the reduced variation in local electrode spacing, which weakens the geometry-induced imbalance in current allocation along the inclined cathode. However, current crowding persists near the sharp cathode edges because of the local concentration of the electric field. This behavior is consistent with the general role of anode geometry reported by Wang et al. [15], although their study also considered vibration-assisted electrolyte flow.

A mesh-sensitivity analysis was conducted for both electrode configurations using the three mesh levels defined in Section 2.2. For the conventional anode, the A_J values obtained using M1, M2, and M3 were 11.51%, 11.66%, and 11.72%, respectively. The corresponding values for the conformal anode were 1.87%, 2.00%, and 2.09%. The primary AJ values reported in Figure 3c were obtained using M1, whereas M2 and M3 were used to evaluate mesh sensitivity. Between M2 and M3, the maximum relative changes in current density at the seven measurement positions within s = 5–35 mm were 2.53% and 2.41% for the conventional and conformal anodes, respectively. The results indicate relatively low mesh sensitivity within the measured inner region. However, the current-density magnitudes at the sharp cathode endpoints increased markedly with mesh refinement. Therefore, the quantitative comparison focuses on the inner region, while edge-current concentration is assessed qualitatively.

3.2. Influence of the Conformal Anode on Grit-Free Metallic Coating-Thickness Dispersion

Grit-free metallic coatings were prepared with the conventional and conformal configurations and measured at seven positions within s = 5–35 mm (Figure 3d). For the conventional anode, thickness ranged from 11.0 to 12.6 μm, with a mean of 11.63 μm. For the conformal anode, thickness ranged from 11.3 to 12.3 μm, with a mean of 11.83 μm. Although their mean thicknesses were similar, the spatial dispersion differed. CV_T decreased from 4.54% with the conventional anode to 2.74% with the conformal anode, corresponding to a relative reduction of approximately 39.7%. Together with the distributions in Figure 3c, these results indicate that the conformal anode reduced mirror asymmetry in the simulated current distribution and thickness dispersion in the measured grit-free inner region.

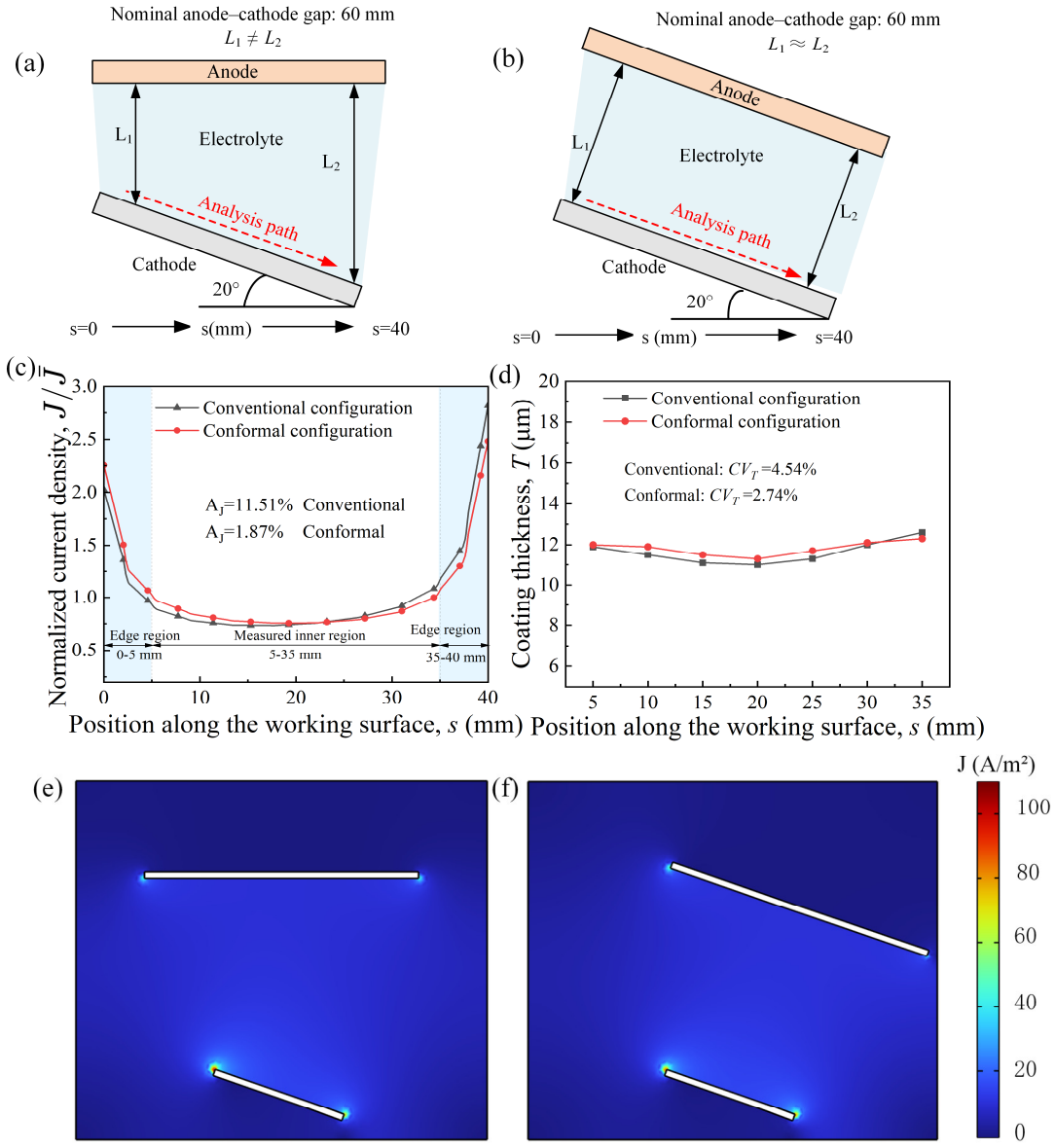


Figure 3. Effects of anode configuration on current distribution and coating thickness in grit-free specimens: (**a**) schematic of the conventional-anode configuration; (**b**) schematic of the conformal-anode configuration; (**c**) simulated normalized current-density profiles along the cathode working surface; (**d**) measured coating-thickness distributions at seven positions (s = 5–35 mm); (**e**) simulated current-density magnitude distribution for the conventional anode; and (**f**) simulated current-density magnitude distribution for the conformal anode. The current-density maps in (**e**,**f**) use the same color scale (0–110 A/m²).

To directly compare the numerical and experimental results, the simulated current-density magnitudes and measured coating thicknesses at the seven corresponding positions are summarized in Table 3.

Table 3. Comparison of simulated current-density magnitudes and measured coating thicknesses at seven positions along the cathode working surface.

s (mm)	J_{conv} (A/m²)	T_{conv} (μm)	J_{conf} (A/m²)	T_{conf} (μm)
5	18.062	11.9	20.064	12.0
10	14.964	11.5	16.242	11.9
15	14.286	11.1	15.101	11.5

20	14.464	11.0	14.842	11.3
25	15.350	11.3	15.255	11.7
30	17.276	12.0	16.597	12.1
35	22.726	12.6	21.010	12.3

Note: J and T represent the simulated current-density magnitude and measured coating thickness, respectively. Subscripts conv and conf denote conventional- and conformal-anode configurations. The simulated current-density values were obtained using the fine mesh (M1).

The simulated current-density profiles and measured coating thicknesses exhibited similar spatial trends, with lower values near the middle of the working surface and higher values toward both sides (Table 3). However, the simulations covered the entire s = 0–40 mm working surface, whereas the thickness measurements were restricted to s = 5–35 mm. The pronounced current-density peaks predicted near the sharp cathode edges were therefore not verified by thickness measurements. Accordingly, the reported CV_T values characterize only the measured inner region and should not be interpreted as evidence of coating-thickness uniformity over the entire working surface. Furthermore, the numerical model did not account for electrodeposition kinetics or coating growth, and the grit-free results cannot be directly extended to the final diamond-containing composite working layer.

3.3. Preliminary Selection of Grit Placement and Nominal Circulation Velocity

To establish common conditions for comparing current-loading schedules, horizontal and inclined grit-placement arrangements were first evaluated, followed by three nominal electrolyte circulation velocities. All screening experiments used the conformal anode and a constant grit-fixation current density of 0.5 A/dm² for 120 min. After preplating, grit placement, fixation, and removal of loose grits, all specimens were thickened for 8 h at 1.0 A/dm² before grit counting and morphological measurements. Nominal circulation velocity refers to the initial pump-outlet velocity defined in Section 2.3.

At a nominal circulation velocity of 0.5 m/s, the mean grit counts across five regions were 64.0 and 65.2 for horizontal and inclined placement, respectively. The corresponding CV_N values were 3.56% and 3.13% (Figure 4a,b). Since inclined placement yielded somewhat lower spatial count dispersion, it was selected for subsequent experiments to match the 20° working-surface orientation. The inclined-placement results at 0.5 m/s were also used as the baseline for the circulation-velocity comparison; these are the same data, not an independent experimental repeat.

For inclined grit placement, nominal circulation velocities of 0.5, 1.5, and 2.5 m/s yielded mean grit counts of 65.2, 66.6, and 62.8, respectively. The corresponding CV_N values were 3.13%, 2.25%, and 3.95%, while the regional grit-height ranges (ΔH_R) were 98.45, 97.58, and 110.62 μm (Figure 4c). Among the three investigated conditions, 1.5 m/s exhibited the lowest grit-count dispersion and regional grit-height range, although the difference in ΔH_R between 0.5 and 1.5 m/s was relatively small. Moderate electrolyte circulation may promote electrolyte renewal and ion transport near the cathode, whereas stronger circulation may disturb the pre-positioned diamond grits before sufficient fixation is achieved. However, neither the local flow field nor grit motion was directly measured, so these explanations remain hypotheses. Therefore, 1.5 m/s was selected as the nominal circulation velocity for the subsequent current-loading comparison in Section 3.4.

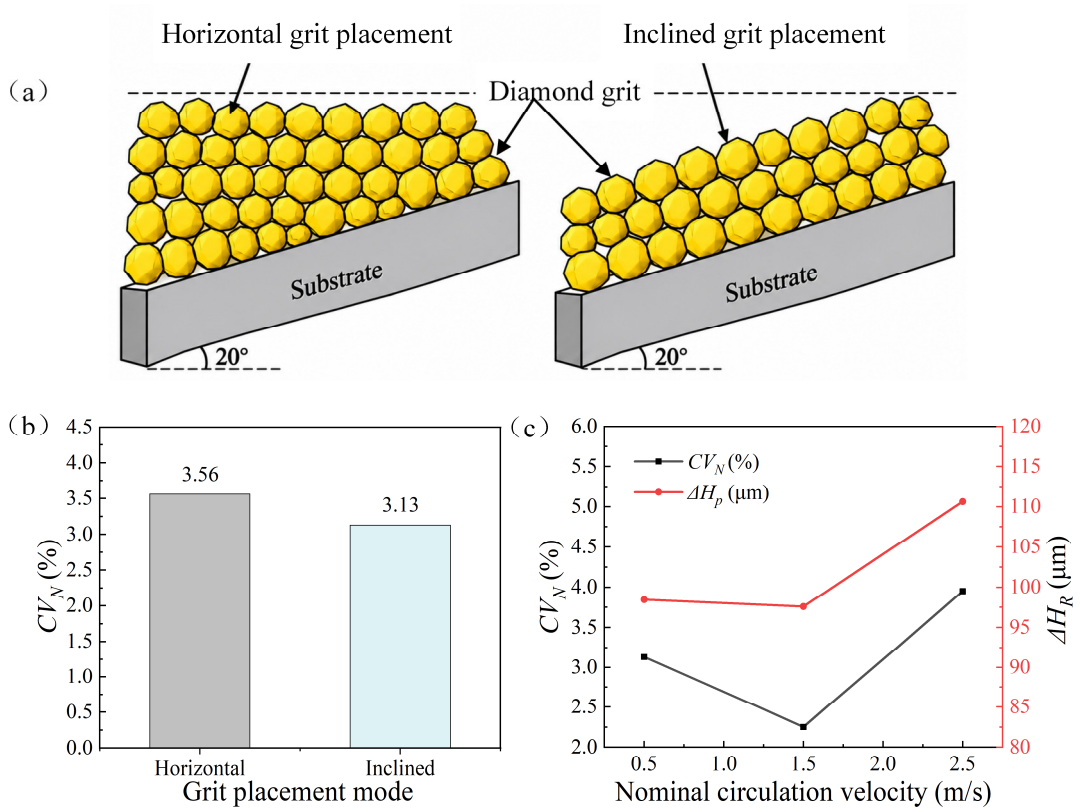


Figure 4. Grit distribution under different pre-positioning methods and nominal circulation velocities: (**a**) schematic of horizontal and inclined grit placement; (**b**) coefficient of variation in grit number under the two placement methods; and (**c**) coefficient of variation in grit number and regional grit-height range at different nominal circulation velocities.

3.4. Effects of Current-Loading Schedules on Final Grit Distribution

Using the inclined grit-placement method and a nominal circulation velocity of 1.5 m/s selected in Section 3.3, the three current-loading schedules were compared under the consistent experimental conditions described in Section 2.3, with three independently prepared specimens for each schedule ($n = 3$).

Representative two-dimensional surface-height maps for the three schedules are presented in Figure 5a–c. The maps were processed using the same height reference, color scale (−150 to 200 μm), and scale bar. The corresponding statistical results are shown in Figure 5d,e. Based on three independent specimens per schedule, the mean CV_N values were 3.16 ± 0.84%, 2.04 ± 0.21%, and 4.28 ± 0.89% for constant-current, stepwise-increasing-current, and step-change-current loading, respectively. The corresponding ΔH_R values were 97.72 ± 4.56, 95.64 ± 1.00, and 103.38 ± 7.39 μm. The results are expressed as mean ± sample standard deviation across the independent specimens. The individual specimen-level CV_N and ΔH_R values for all nine specimens are provided in Table 4. The stepwise-increasing-current group exhibited the lowest mean CV_N, while the specimen-level ΔH_R values showed overlap among the three current-loading schedules.

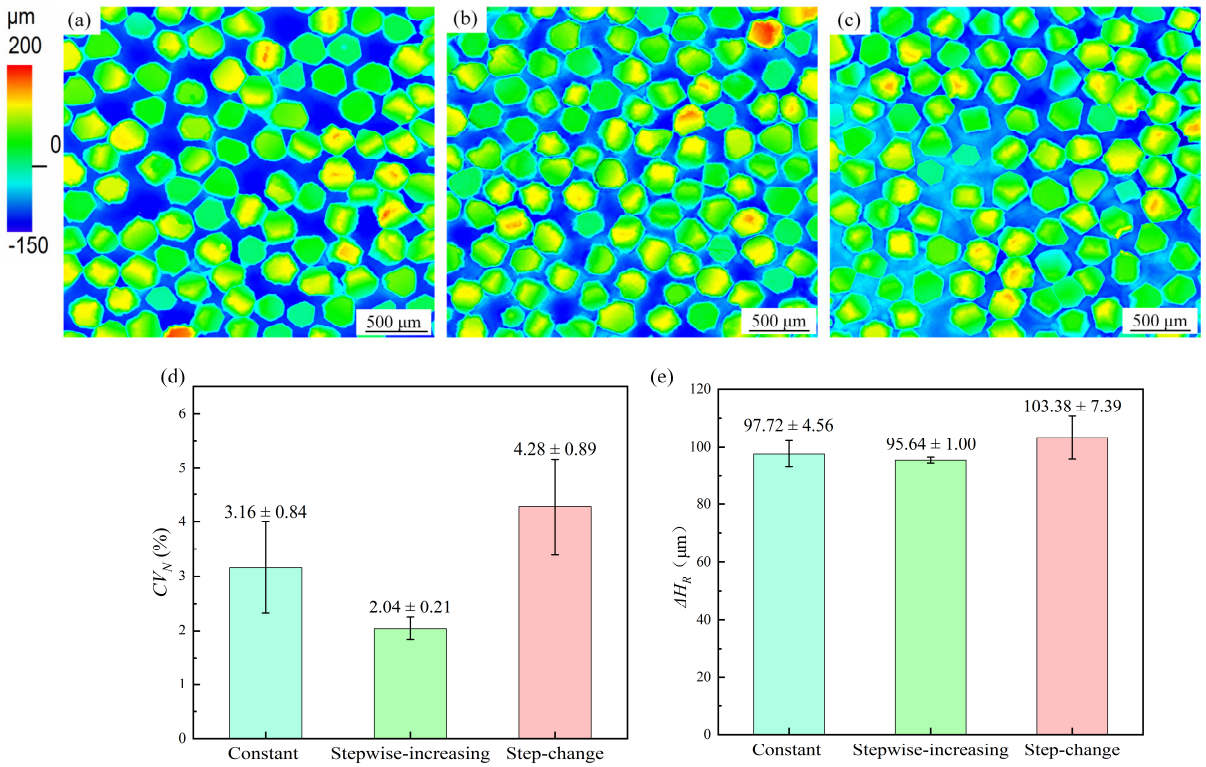


Figure 5. Representative two-dimensional surface-height maps and grit-distribution characteristics obtained under different current-loading schedules: (**a**) constant-current loading; (**b**) stepwise-increasing-current loading; (**c**) step-change-current loading; (**d**) coefficient of variation in grit number (CV_N); and (**e**) regional grit-height range (ΔH_R). Data in (**d**,**e**) are presented as mean ± standard deviation (n = 3 independent specimens per current-loading schedule). The height maps in (**a**–**c**) represent selected measurement regions rather than group averages.

Table 4. Individual specimen-level grit-count coefficients of variation and regional grit-height ranges for the three current-loading schedules.

Current-Loading Schedule	Specimen	CV_N (%)	ΔH_R (μm)
Constant current	C1	3.33	102.35
	C2	3.89	93.24
	C3	2.25	97.58
Stepwise-increasing current	I1	2.28	96.77
	I2	1.89	95.26
	I3	1.95	94.89
Step-change current	S1	4.97	108.02
	S2	4.59	94.86
	S3	3.28	107.25

Note: CV_N was calculated from five nonoverlapping measurement regions within each specimen using the population standard deviation. Specimen C3 was also used in the preliminary circulation screening at 1.5 m/s and was included only once in the constant-current group.

Among the three current-loading schedules, stepwise-increasing current exhibited the lowest mean CV_N and ΔH_R. Compared with constant-current loading, the mean CV_N decreased by approximately 35%, while ΔH_R decreased by 2.08 μm. Relative to step-change-current loading, the corresponding reductions were approximately 52% and 7.74 μm. However, the differences in ΔH_R were less consistent among individual specimens, particularly in comparison with constant-current loading.

The lower observed grit-count dispersion under stepwise-increasing-current loading may be associated with the progressive development of the metallic bond around pre-positioned diamond grits. The initial low-current stage may allow gradual bond formation, while subsequent increases in current density may promote further metal deposition around the grit bases. Previous studies have also shown that current-loading sequences can influence electrodeposition outcomes [28,34]. However, the grit–metal interface was not directly observed during fixation. Moreover, the three schedules differed in fixation duration and mean current density, and all specimens underwent the same subsequent thickening process. Therefore, the observed differences cannot be attributed solely to the current sequence.

Representative SEM side-view morphologies of the diamond composite working layers are presented in Figure 6. The low-magnification images (Figure 6a–c) show multiple polyhedral diamond grits protruding from the working surface, with metallic material surrounding their lower portions. The higher-magnification images (Figure 6d–f) further reveal the local encapsulation morphology around the diamond grit bases, while the exposed crystal facets retain their characteristic geometry. These observations complement the surface-height characterization in Figure 5 and provide additional qualitative evidence of the morphological characteristics of the electrodeposited diamond composite working layers. The comparative evaluation of the three current-loading schedules is based on the quantitative results presented in Figure 5.

Overall, the repeated experiments indicate a tendency toward lower spatial grit-count dispersion under stepwise-increasing-current loading within the investigated conditions. However, the limited number of independent specimens restricts the generalizability of this finding. The measured results characterize the final grit distribution and regional surface-height variation rather than grit-retention strength or dressing performance.

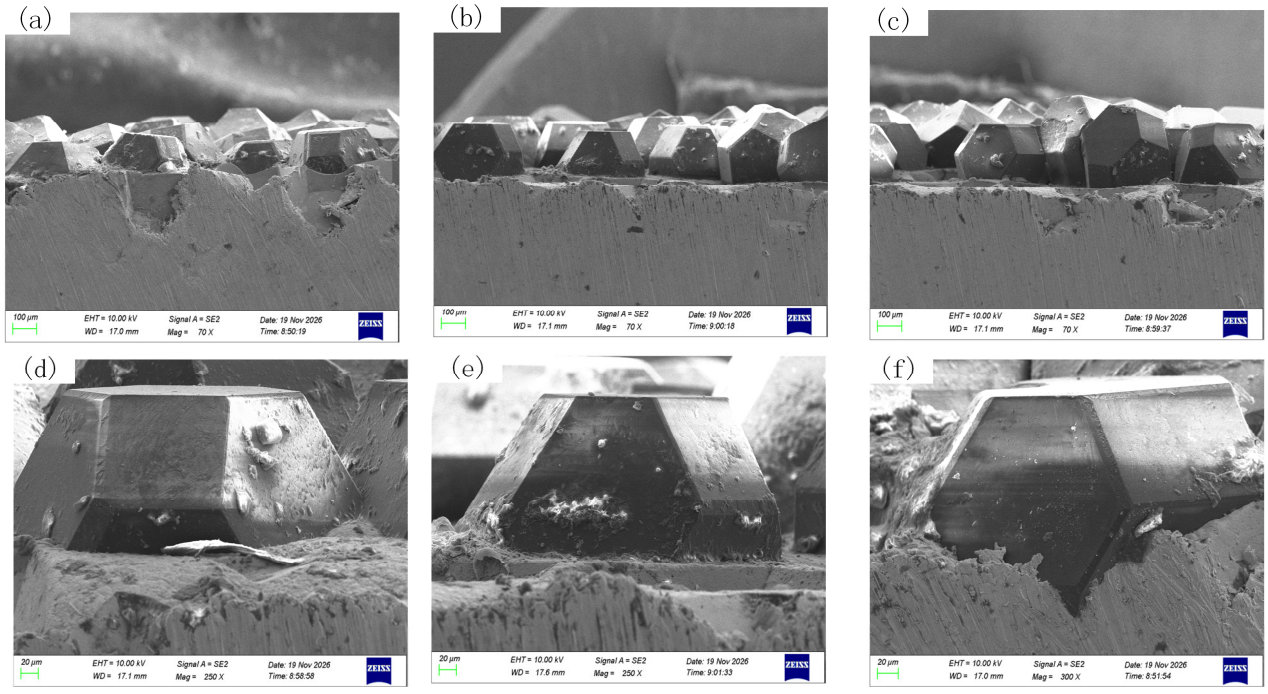


Figure 6. SEM side-view morphologies of the diamond composite working layers: (**a–c**) overall grit morphologies at low magnification; (**d–f**) local morphologies around the diamond grit bases at higher magnifications.

3.5. Grit-Distribution Assessment of the Actual Double-Working-Surface Diamond Dressing Roller

The conformal-anode and stepwise-increasing-current process was applied to an actual double-working-surface dressing roller as described in Section 2.4. Grit-number distributions and representative local surface morphology were then characterized (Figure 7). Five equal-area counting regions were selected on each of Working surface I and Working surface II, using the same grit-counting rule.

The grit counts were relatively concentrated within the measured regions of both surfaces (Figure 7b). The mean counts were 64.0 and 64.8 on Working surface I and Working surface II, with CV_N values of 1.40% and 1.15%, respectively. Thus, both working surfaces exhibited relatively low spatial grit-count dispersion across the selected regions.

Three-dimensional surface morphology and a two-dimensional height map from a representative region are presented in Figure 7c,d. The regional grit-height range (ΔH_R), obtained from the difference between the maximum and minimum valid grit-surface heights, was 95.45 μm. This value was close to the mean ΔH_R of 95.64 ± 1.00 μm obtained from three independently prepared inclined specimens under stepwise-increasing-current loading. However, the actual roller underwent 20.5 h of constant-current thickening after initial grit fixation, compared with 8 h for the inclined specimens. Therefore, the similarity in regional height ranges should be interpreted as a descriptive observation rather than evidence of equivalent grit-height distributions or identical fixation behavior. The measured grit-count and surface-morphology results support the feasibility of applying the combined process to the investigated double-working-surface geometry.

https://doi.org/10.3390/mi17121391

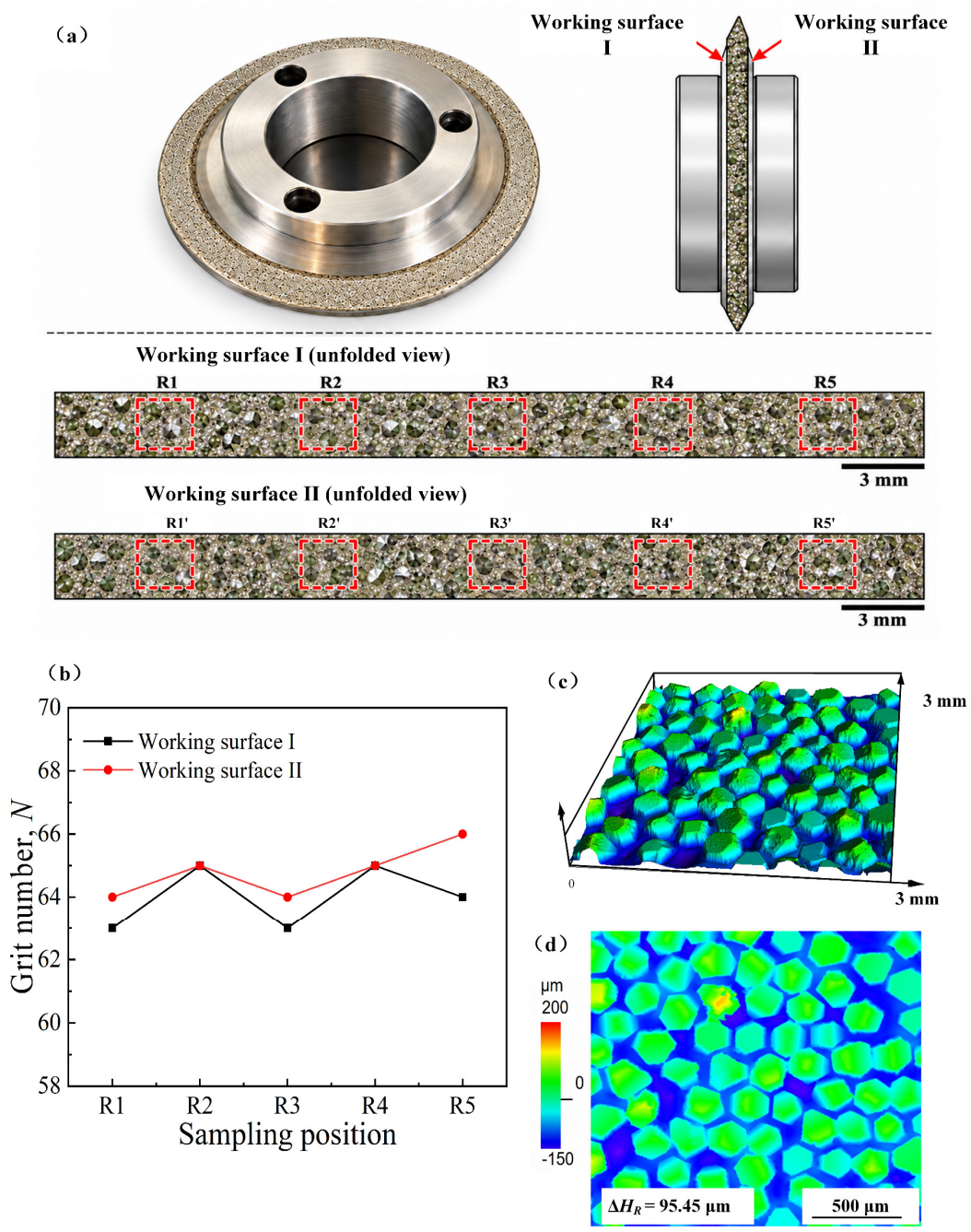


Figure 7. Grit distribution and surface morphology of the fabricated double-working-surface diamond dressing roller: (**a**) roller structure and measurement regions(red dashed squares indicate the regions selected for grit counting); (**b**) grit-number distribution on the two working surfaces; (**c**) three-dimensional topography of a representative region; and (**d**) two-dimensional height map and regional grit-height range of that region.

4. Conclusions

This study investigated a combined conformal-anode and stepwise-increasing-current strategy for improving the electrodeposition uniformity of nickel-based diamond working layers on inclined surfaces. Numerical simulations, electrodeposition experiments, and fabrication of a double-working-surface diamond dressing roller were conducted to evaluate current distribution, coating thickness, and diamond grit distribution. The main conclusions are summarized as follows:

(1) The conformal anode reduced current-density mirror asymmetry on the inclined working surface, with A_J decreasing from 11.51% to 1.87%. In the grit-free coating experiments, the coefficient of variation in coating thickness (CV_T) within the measured inner region decreased from 4.54% to 2.74%, corresponding to a relative reduction of approximately 39.7%. However, current crowding near the electrode edges was not eliminated.

(2) Among the three nominal electrolyte circulation velocities investigated in the preliminary screening, 1.5 m/s yielded the lowest measured grit-count dispersion (CV_N = 2.25%) and regional grit-height range (ΔH_R = 97.58 μm). This condition was selected for the subsequent comparison of current-loading schedules. The observed trend may be associated with the competing effects of electrolyte renewal and disturbance of pre-positioned diamond grits.

(3) Based on three independent specimens per current-loading schedule, the mean CV_N values were 3.16 ± 0.84%, 2.04 ± 0.21%, and 4.28 ± 0.89% for constant-current, stepwise-increasing-current, and step-change-current loading, respectively. The corresponding ΔH_R values were 97.72 ± 4.56, 95.64 ± 1.00, and 103.38 ± 7.39 μm. The stepwise-increasing-current schedule exhibited the lowest mean values for both indicators. Its grit-fixation duration was 80.4 min, approximately 33% shorter than the 120 min constant-current schedule. These results characterize the compared processing schedules rather than the isolated effect of current sequence.

(4) A double-working-surface diamond dressing roller was successfully fabricated using the combined conformal-anode and stepwise-increasing-current process. The CV_N values of the two working surfaces were 1.40% and 1.15%, respectively, and the regional grit-height range in a representative region was 95.45 μm. These results demonstrate the feasibility of applying the combined process to the selected complex-profile geometry and provide information on the grit distribution and surface morphology of the fabricated roller.

Several limitations should be acknowledged. The numerical model did not explicitly consider electrochemical kinetics or coating growth, and the experimental investigation was limited to the selected 20° geometry. The quantitative comparison of coating thickness between the two anode configurations was limited to grit-free specimens, while the SEM observations provided only qualitative morphological information on the diamond composite working layers. The final grit distributions also reflected the subsequent thickening process. Furthermore, the fabricated roller was evaluated primarily through surface-morphology measurements rather than direct dressing-performance tests. Further investigations are therefore needed to assess the general applicability of the process and its influence on grit retention, dressing accuracy, and tool service life.

Author Contributions: Formal analysis, H.L., W.Y. and C.W.; Investigation, Z.Y.; Writing—original draft preparation, H.L.; Writing—review and editing, P.M. All authors have read and agreed to the published version of the manuscript.

Funding: This research was funded by the Henan Provincial Key Research and Development Program [No.251111230800].

Institutional Review Board Statement: Not applicable.

Informed Consent Statement: Not applicable.

Data Availability Statement: The original contributions presented in the study are included in the article; further inquiries can be directed to the corresponding author.

Conflicts of Interest: The authors declare no conflicts of interest.

References

1. Wu, H. Wire sawing technology: A state-of-the-art review. *Precis. Eng.* **2016**, *43*, 1–9. https://doi.org/10.1016/j.precisioneng.2015.08.008.
2. Sefene, E.M.; Chen, C.C.A.; Tsai, Y.H. A comprehensive review of diamond wire sawing process for single-crystal hard and brittle materials. *J. Manuf. Process.* **2024**, *131*, 1466–1497. https://doi.org/10.1016/j.jmapro.2024.09.093.
3. Ge, M.; Zhang, C.; Wang, P.; Li, Z.; Ge, P. Modeling of electroplated diamond wire and its application towards precision slicing of semiconductors. *J. Manuf. Process.* **2023**, *87*, 141–149. https://doi.org/10.1016/j.jmapro.2023.01.003.
4. Huang, C.A.; Yang, S.W.; Shen, C.H.; Cheng, K.C.; Wang, H.; Lai, P.L. Fabrication and evaluation of electroplated Ni-diamond and Ni-B-diamond milling tools with a high density of diamond particles. *Int. J. Adv. Manuf. Technol.* **2019**, *104*, 2981–2989. https://doi.org/10.1007/s00170-019-04174-3.
5. Huang, C.A.; Shen, C.H.; Li, P.Y.; Lai, P.L. Effect of fabrication parameters on grinding performances of electroplated Ni-B-diamond tools with D150-diamond particles. *J. Manuf. Process.* **2022**, *80*, 374–381. https://doi.org/10.1016/j.jmapro.2022.05.055.
6. Shen, C.H.; Rodchanarowan, A.; Li, P.Y.; Huang, C.C.; Chen, Y.C.; Lai, P.L.; Huang, C.A. Grinding performances and failure analyses of electroplated Ni-B-diamond tools with a high density of single- or dual-layer D-150-diamond particles. *Int. J. Adv. Manuf. Technol.* **2024**, *131*, 3739–3750. https://doi.org/10.1007/s00170-024-13205-7.
7. Khosravi, J.; Azarhoushang, B.; Behjat, S.; Zahedi, A. Investigating a novel and highly efficient approach for the fabrication of diamond profile rollers using wire electrical discharge conditioning (WEDC). *Int. J. Adv. Manuf. Technol.* **2024**, *134*, 3937–3950. https://doi.org/10.1007/s00170-024-14335-8.
8. Aleksandrova, I.; Mitev, H. Investigation and Modelling of the Wear Resistance of Diamond Roller Dressers Made of Synthetic Diamonds with Mixed Grit Size. *Coatings* **2025**, *15*, 1376. https://doi.org/10.3390/coatings15121376.
9. Li, C.; Sun, L.; Yang, S.; Zhang, L.; Wu, C.; Jiang, Z. Three-dimensional characterization and modeling of diamond electroplated grinding wheels. *Int. J. Mech. Sci.* **2018**, *144*, 553–563. https://doi.org/10.1016/j.ijmecsci.2018.06.010.
10. Fang, X.; Wang, S.; Li, B.; Wu, J.; Hong, Z.; Pan, R.; Du, L.; Wang, J. Full-field characterization of electroplated diamond grinding wheel abrasive protrusion height based on image processing. *Meas. Sci. Technol.* **2026**, *37*, 045408. https://doi.org/10.1088/1361-6501/ae3a06.
11. Yang, J.M.; Zhu, D.; Wang, K. Application of a novel conformal anode in electroforming complex revolving parts. *Electromachining Mould.* **2004**, *5*, 23–25, 66. (In Chinese)
12. Yang, J.M.; Zhu, D.; Wang, K. Quality control of nickel–manganese alloy electroforming for thin-walled revolving parts. *Trans. Chin. Soc. Agric. Mach.* **2007**, *38*, 177–180. (In Chinese)
13. Yang, J.M.; Kim, D.H.; Zhu, D.; Wang, K. Improvement of deposition uniformity in alloy electroforming for revolving parts. *Int. J. Mach. Tools Manuf.* **2008**, *48*, 329–337. https://doi.org/10.1016/j.ijmachtools.2007.10.006.
14. Zhu, Z.W.; Zhu, D.; Qu, N.S.; Wang, K.; Yang, J.M. Electroforming of revolving parts with near-polished surface and uniform thickness. *Int. J. Adv. Manuf. Technol.* **2008**, *39*, 1164–1170. https://doi.org/10.1007/s00170-007-1300-9.
15. Wang, Z.; Zhu, Z.; Zhu, D. Simulation and experimental study of anode vibration-assisted electroforming of complex thin-walled components. *Int. J. Electrochem. Sci.* **2026**, *21*, 101382. https://doi.org/10.1016/j.ijoes.2026.101382.
16. Mehdizadeh, S.; Dukovic, J.; Andricacos, P.C.; Romankiw, L.T.; Cheh, H.Y. Optimization of electrodeposit uniformity by the use of auxiliary electrodes. *J. Electrochem. Soc.* **1990**, *137*, 110–117. https://doi.org/10.1149/1.2086343.
17. Park, C.W.; Park, K.Y. An effect of dummy cathode on thickness uniformity in electroforming process. *Results Phys.* **2014**, *4*, 107–112. https://doi.org/10.1016/j.rinp.2014.07.004.
18. Zhao, M.; Du, L.; Wei, Z.; Du, C.; Liu, X.; Ji, X. Fabrication of metal microfluidic chip mold with coplanar auxiliary cathode in the electroforming process. *J. Micromech. Microeng.* **2019**, *29*, 025002. https://doi.org/10.1088/1361-6439/aaf605.
19. Wang, H.; Xing, J.; Fan, T.; Liu, J.; Xie, J.; Li, C. An effect of layered auxiliary cathode on thickness uniformity in micro electroforming process. *Micromachines* **2023**, *14*, 1307. https://doi.org/10.3390/mi14071307.
20. Lee, J.M.; Hachman, J.T.; Kelly, J.J.; West, A.C. Improvement of current distribution uniformity on substrates for microelectromechanical systems. *J. Micro/Nanopatterning Mater. Metrol.* **2004**, *3*, 146–151. https://doi.org/10.1117/1.1631924.
21. Ahmadkhaniha, D.; Sieber, M.; Zanella, C. Controlling coating thickness distribution for a complex geometry with the help of simulation. *Int. J. Adv. Manuf. Technol.* **2024**, *134*, 3703–3717. https://doi.org/10.1007/s00170-024-14337-6.
22. Noack, M.; Maier, R.; Kirchner, E. Finite Element Simulation and Experimental Validation of Nickel Coating Thickness Distribution in Electroplated FCCZ Lattice Structures. *J. Compos. Sci.* **2026**, *10*, 24. https://doi.org/10.3390/jcs10010024.
23. Cao, Q.D.; Fang, L.; Lv, J.M.; Zhang, X.P.; Dat, N.T. Effects of pulse reverse electroforming parameters on the thickness uniformity of electroformed copper foil. *Trans. IMF* **2018**, *96*, 108–112. https://doi.org/10.1080/00202967.2018.1423736.

24. Chen, C.; Liu, J.; Song, K. Optimizing thickness uniformity in double-pulse nickel electroforming via a physics-guided COMSOL–ANN–WOA framework. *Proc. Inst. Mech. Eng. Part E J. Process Mech. Eng.* **2026**, *advance online publication*. https://doi.org/10.1177/09544089261419665.
25. Lee, W.H.; Tang, S.C.; Chung, K.C. Effects of direct current and pulse-plating on the co-deposition of nickel and nanometer diamond powder. *Surf. Coat. Technol.* **1999**, *120*, 607–611. https://doi.org/10.1016/S0257-8972(99)00445-4.
26. Yang, Y.; Cheng, Y.F. Fabrication of Ni-Co-SiC composite coatings by pulse electrodeposition—Effects of duty cycle and pulse frequency. *Surf. Coat. Technol.* **2013**, *216*, 282–288. https://doi.org/10.1016/j.surfcoat.2012.11.059.
27. Zhang, X.; Qin, J.; Perasinjaroen, T.; Aeksen, W.; Das, M.K.; Hao, R.; Zhang, B.; Wangyao, P.; Boonyongmaneerat, Y.; Limpanart, S.; et al. Preparation and hardness of pulse electrodeposited Ni-W-diamond composite coatings. *Surf. Coat. Technol.* **2015**, *276*, 228–232. https://doi.org/10.1016/j.surfcoat.2015.06.073.
28. Srimaneerat, J.; Kothanam, N.; Moolla, P.; Wintachai, P.; Triroj, N.; Harachai, K.; Jaroenapibal, P. Advancing Ni-W/diamond coatings with pulse-brush plating: Insights into particle incorporation and hardness. *Diam. Relat. Mater.* **2025**, *157*, 112472. https://doi.org/10.1016/j.diamond.2025.112472.
29. Sajjadnejad, M.; Omidvar, H.; Javanbakht, M.; Mozafari, A. Textural and structural evolution of pulse electrodeposited Ni/diamond nanocomposite coatings. *J. Alloys Compd.* **2017**, *704*, 809–817. https://doi.org/10.1016/j.jallcom.2016.12.318.
30. Lajevardi, S.A.; Shahrabi, T.; Szpunar, J.A. Synthesis of functionally graded nano Al_2O_3-Ni composite coating by pulse electrodeposition. *Appl. Surf. Sci.* **2013**, *279*, 180–188. https://doi.org/10.1016/j.apsusc.2013.04.067.
31. Yang, X.H.; Zhang, X.M.; Ming, P.M.; Li, Y.T.; Wang, W.; Zhang, Y.Y.; Li, Z.B.; Li, L.X.; Xiao, Y.P.; Guo, X.Y.; et al. Fabricating ultra-narrow precision slit structures with periodically reducing current over-growth electroforming. *Micromachines* **2024**, *15*, 76. https://doi.org/10.3390/mi15010076.
32. Kim, M.J.; Choe, S.; Kim, H.C.; Lee, S.J.; Kim, S.H.; Kwon, O.J.; Kim, J.J. Cu direct electrodeposition using step current for superfilling on Ru-Al_2O_3 layer. *Electrochim. Acta* **2014**, *147*, 371–379. https://doi.org/10.1016/j.electacta.2014.09.142.
33. Kim, H.C.; Kim, M.J.; Seo, Y.; Lee, Y.; Choe, S.; Kim, Y.G.; Cho, S.K.; Kim, J.J. Bottom-up filling of TSV-scaled trenches by using step current electrodeposition. *ECS Electrochem. Lett.* **2015**, *4*, D31–D34. https://doi.org/10.1149/2.0061510eel.
34. Shen, K.; Xiong, Z.; Li, Y.; Wu, X.; Staiger, M.; Bai, J.; Liu, Z.; Giyasov, S.; Nuriddinov, K.Z.; Lv, S.; et al. Microstructure tailoring of micro-reentrant Cu coatings via stepwise electrodeposition with enhanced mechanical properties and corrosion resistance. *Mater. Charact.* **2026**, *240*, 116785. https://doi.org/10.1016/j.matchar.2026.116785.
35. *GB/T 12332-2008*; Metallic Coatings—Electroplated Coatings of Nickel for Engineering Purposes. Standardization Administration of China: Beijing, China, 2008.
36. *GB/T 12611-2008*; Technical Requirements of Quality Control for Metal Parts to Be Coated. Standardization Administration of China: Beijing, China, 2008.

Disclaimer/Publisher's Note: The statements, opinions and data contained in all publications are solely those of the individual author(s) and contributor(s) and not of MDPI and/or the editor(s). MDPI and/or the editor(s) disclaim responsibility for any injury to people or property resulting from any ideas, methods, instructions or products referred to in the content.